Linear MHD analyses of locked-mode-like instabilities in LHD

Linear MHD analyses of locked-mode-like instabilities in LHD

M. Okamoto[1], H. Tomita[2], K.Y. Watanabe[2,3], M. Sato[3], Y. Takemura[3,4], S. Sakakibara[3,4], K. Ida[3,4], M. Yoshinuma[3] and LHD experiment group

1) National Institute of Technology, Ishikawa College, Kitachujo, Tsubata, Kahoku-gun, Ishikawa 929-0392, Japan
2) Nagoya University, Graduate School of Engineering, Chikusa, Nagoya 464-8603, Japan
3) National Institute for Fusion Science, National Institutes of Natural Science, Toki, Gifu 509-5292, Japan
4) SOKENDAI (The Graduate University for Advanced Studies), Toki, Gifu 509-5292, Japan

Abstract
In order to investigate the driving mechanism of the locked-mode-like instability observed in the LHD (Large Helical Device), we reconstruct the MHD equilibria consistent with the measurement and identify a dominant MHD instability in the precursor phase based on linear MHD analyses. From the dependence of the linear growth rate on Magnetic Reynolds number, the radial mode structure of the electrostatic potential fluctuation and other indices, the ideal interchange mode is found to be dominant. Moreover, it is found that Mercier parameter, D_I, becomes much larger than 0.3 during the phase while the precursor has constant frequency and fluctuation amplitude. Therefore, $D_I>>0.3$ is a good index of the on-set condition of the minor collapse itself. It is also found that the achievement of $D_I>>0.3$ is due to the movement of the resonant surface to the inner plasma region, which corresponds to the larger pressure gradient region.

1. Introduction

In the toroidal magnetic confinement devices, the stable sustainment of high beta plasma is one of the important issues for the achievement of the nuclear fusion power plant. The achievable beta is limited by the plasma current and pressure driven magnetohydrodynamic (MHD) instabilities. The minor collapse and disruption are driven by MHD instabilities in tokamak plasmas, which limit the achievable beta value.

In the Large Helical Device (LHD) [1], which is a typical heliotron device, the existence of MHD activities and a small flattening region in the electron temperature profile have been reported in the reactor-relevant high beta discharges, which do not lead to the collapse in the pressure profile and any disruptive phenomena [2]. However, in the low magnetic shear configurations with a co-plasma current, a collapse of the pressure profile is observed even in the relatively low beta discharges [3]. Here, the co-plasma current is driven by the neutral beam current drive (NBCD), and the co-direction corresponds to the enhancement of the rotational transform. In the above collapse discharges, the "locked-mode-like instabilities" are observed [4]. The instability has a precursor whose frequency decreases and its fluctuation amplitude increases before the pressure collapse. The above behavior resembles that of the locked-mode in tokamaks [5]. There are many previous experimental works on the radial mode structure of the precursor of the locked-mode-like instability, the slowing-down behavior of the mode frequency and the slowing-down mechanism of the mode frequency [4, 6-10]. The following results are obtained: (1) the mode frequency of the precursor is almost the same with the ExB plasma rotation frequency at the resonant surface. (2) There are two types of locked-mode-like instabilities. One instability has the interchange parity in the radial structures of the internal fluctuation such as the electron temperature, and the other has the tearing parity. (3) The slowing-down rate of the precursor's frequency grows larger as the imposed resonant error field increases.

On the previous numerical analysis of the driving mechanism, there are few because the plasma current profile significantly affects the stability evaluation, but the identification in the experiments was difficult [11]. In this paper, we reconstruct the MHD equilibria consistent with some discharges of the locked-mode-like instabilities with the internal mode structure of the interchange parity based on the measurement of the rotational transform, and also on the electron temperature and density profiles. We apply the local stability analysis on the ideal interchange instability and the tearing

mode such as Mercier parameter (D_I) and Δ', and the global linear stability analysis based on the reduced MHD equation.

This paper is organized as follows. In section 2, the experimental setup is explained. In sections 3 and 4, the numerical analysis results and the discussion appear. Finally, the paper is summarized in section 5.

2. Experiment setup

The MHD stability of the LHD is strongly affected by the pressure and plasma current profiles. Then it is important to reconstruct the MHD equilibria to be consistent with the experiments. In an earlier analysis [11], we had evaluated the equilibrium by using the measured kinetic plasma pressure profile, which is measured by Thomson scattering and FIR interferometer, and the rotational transform profile with the assumed parabolic current density profile and the observed net toroidal current by the Rogowski coils [12]. In this study, we evaluate the rotational transform profile of the discharges with the locked-mode-like instabilities by using motional Stark effect (MSE) diagnostic [13].

Figure 1 shows a typical radial profile of (a) the electron temperature T_e, (b) the toroidal current density j_p, (c) the rotational transform $\iota/2\pi$ and (d) Mercier parameter D_I of a discharge with the locked-mode-like instability. In Fig.1 (a), the open circles and the solid line denote the temperature and its fitting curve, respectively. In Figs.1 (b), (c) and (d), the solid lines with open triangle and cross correspond to the assumed parabolic and hollow current profile, respectively. The open square means the rotational transform profile measured by MSE, and the solid line with open circles is the current density and the rotational transform fitted by the MSE data. Here, we show the data without the core region because the MSE system of the LHD has a poor accuracy on the measurement in the core region [13]. It should be noted that the global mode is numerically well-known to become unstable whenever $D_I > 0.2$ (dashed line in Fig.2(d)) [14], and the yellow band in Fig.1 shows the area around $\iota/2\pi=1$ rational surface. Here D_I is defined as the following expression [14].

$$D_I = D_I^{(shear)} + D_I^{(well)} + D_I^{(J\cdot B)} + D_I^{(G.C.)} \tag{1}$$

$$\left.\begin{aligned} D_I^{(shear)} &= -\frac{1}{4}, \\ D_I^{(well)} &= -\left(p' V'' \left\langle \frac{B^2}{|\nabla\psi|^2} \right\rangle - p'^2 \left\langle \frac{1}{B^2} \right\rangle \left\langle \frac{B^2}{|\nabla\psi|^2} \right\rangle \right) \Big/ \left(\frac{\iota'}{2\pi} \right)^2, \\ D_I^{(J\cdot B)} &= \left\langle \frac{\left(\mathbf{J} - I'\mathbf{B}\right)\cdot\mathbf{B}}{|\nabla\psi|^2} \right\rangle \Big/ \left(\frac{\iota'}{2\pi} \right), \\ D_I^{(G.C.)} &= -\left(\left\langle \frac{\mathbf{J}\cdot\mathbf{B}}{|\nabla\psi|^2} \right\rangle^2 - \left\langle \frac{B^2}{|\nabla\psi|^2} \right\rangle \left\langle \frac{(\mathbf{J}\cdot\mathbf{B})^2}{|\nabla\psi|^2} \right\rangle \right) \Big/ \left(\frac{\iota'}{2\pi} \right)^2. \end{aligned}\right\} \tag{2}$$

where ' denotes the derivative respect to ψ. ψ, V, p, **J**, **B** and I are the toroidal magnetic flux, the plasma volume, the equilibrium plasma pressure, the plasma current density, the magnetic field and the net toroidal current, respectively. From Fig.1, it is found that the location of the resonant surface and its D_I value strongly depend on the current density profile. Thus, the accurate identification of the current density profile is important to precisely evaluate D_I. We determine the current density profile in such a way as to fit the rotational transform profile measured by MSE diagnostic such as the solid line with open circles of Fig. 1(b) and (c). Here the plasma current is evaluated so that the rotational transform of MHD equilibrium calculated by the VMEC code [15] under the assumed plasma current is fitted with that by the MSE diagnostics.

Figure 2 shows the typical waveform of the discharge with the locked-mode-like instability. The locked-mode-like instabilities are observed in the low magnetic shear discharges with the co-plasma current. The plasma current I_p is generated by unbalanced tangential Neutral Beam (NB) injection. In the LHD, the higher the plasma aspect ratio A_p is, the lower the magnetic shear becomes. Here A_p is set at 7.1, which corresponds to higher aspect ratio configuration compared with reactor relevant high-beta discharges of the LHD [16]. The current profile in Fig.1 (b) corresponds to the data at t=3.9s in the waveform of Fig.2. In this discharge, the NBCD current is expected to be more dominant than the

bootstrap current. Though the heating profile of the tangential NB is center-peaked, the current profile consistent with MSE measurement has the off-axis peaked profile. The reason is that t=3.9s corresponds to 0.6s after the NB injection as shown in Fig.2, which is less than the L/R time, and that induces an inductive current, which leads to the off-axis peaked current profile. The other experimental conditions are as follows: the major radius of the magnetic axis location R_{ax} = 3.6 m, B_t = 1.27 T, which is the toroidal field at R_{ax}. Figures 2(a), (b), (c), (d), (e) and (f) show the time evolution of the volume averaged beta value, the normalized plasma current by B_t, the central electron temperature, the line averaged density, the amplitude and the frequency of m/n=1/1 poloidal magnetic fluctuation with relatively high frequency normalized by B_t, the amplitude of m/n=1/1 radial magnetic fluctuation with low frequency and D_I, respectively. It should be noted that the magnetic fluctuations with relatively high frequency and low frequency are measured by magnetic probes and saddle loops, respectively.

The hydrogen gas, which is working gas, is supplied at t= 3.5~4.5 sec and NB injection is applied at t= 3.3~4.8 sec. A neon gas puff is applied at t= 3.5~3.6 sec to increase the ramp-up rate of plasma current. The minor collapse occurs approximately at t = 4.36 sec, I_p/B_t ~ 39 kA/T, and the volume averaged beta $<\beta>$ = 1.0 %. From Fig. 2 (b), it should be noted that $<\beta>$ and line averaged electron density approximately at t = 3.85 sec would slightly increase due to a 'transition' [17, 18]. The transition is called the L-H transition in helical plasmas, and it has the following characteristics: the edge density gradient suddenly increases, and the particle confinement is apparently improved. From the time evolution of the beta value and the amplitude of the magnetic fluctuation in Fig. 2 (a) and (c), the discharge with the locked-mode-like instability is divided into the following 4 phases [10]. In the initial phase of the discharge, the precursor hardly appears, which corresponds to the phase (I). Next, the precursor clearly appears, and its amplitude is almost constant in the phase (II). In the phase (III), the amplitude of the precursor increases, and the beta value gradually decreases. Here it should be noted that the frequency of the precursor in the phase (II) is constant, and that in the phase (III) decreases to zero as shown in Fig.2 (d). After the frequency becomes zero, the non-rotating magnetic fluctuation rapidly grows and the beta value also rapidly decreases, which corresponds to the phase (IV). In the phase (IV), the amplitude of the precursor cannot be measured by the magnetic probes because the rotation stops. In the discharges with the locked-mode-like instability, we cannot observe core resonant modes such as m/n=2/1 before the collapse as shown in refs.[4, 6].

We use the MSE diagnostic with the sampling time of 0.3 sec to measure the rotational transform profile. Thus, we can evaluate three points of D_I before the collapse as shown in Fig.2 (e), which means that we can obtain usually one MSE data in a phase every discharge. On the evaluation of the rotational transform by MSE in the LHD, we assume the nest magnetic surfaces of the MHD equilibria. Then we cannot evaluate the rotational transform profile and D_I with accuracy in the phase (IV) because in the phase (IV), the large magnetic island is expected to be formed. In the discharge of Fig.2, it is found that the phase (I) leads to be stable for the global ideal interchange mode, the phase (II) and (III) are unstable and stable, respectively.

3. Analysis results

To obtain data at the many time slices and with various experimental conditions for the investigation of the time evolution behavior of D_I during the precursor phase of the locked-mode-like instabilities, we perform several discharges in which an amount of neon gas puffing and the measurement timing of MSE diagnostic are changed. In Fig. 3, (a) the amplitude of m/n = 1/1 precursor magnetic fluctuation and (b) evaluated D_I are plotted in the three phases as shown in Fig.2, where the amplitude of the magnetic fluctuation is the time-averaged value over the 0.1 sec period. The horizontal axis corresponds to the normalized plasma current by B_t, and the dashed line and the dotted-dashed line denote D_I=0.2 and 0.3, respectively. It should be noted that the data in Fig.3 consists of 8 discharges with different current ramp-up rates and/or MSE measurement timing. Then the plasma current monotonically increases with each discharge duration time in this experiment series, but the plasma current value does not coincide with the discharge duration time. In the phase (I), the mode amplitude is exceedingly small compared with other phases. Mercier criterion is in stable condition such as in the phase (I) of Fig.2, and D_I tends to increase with the increase of the plasma current. In the phase (II), the magnetic fluctuation is clearly observed, and the amplitude is almost constant. The value of

D_I becomes large during the initial phase of phase (II). It decreases with the increase of I_p. The value of D_I should be noted that D_I is less than 0.3 in the quasi-steady state of the LHD discharges according to the early works [19, 20]. In the phase (III), the amplitude is increased with the increase of I_p. On the other hand, D_I decreases until the occurrence of the collapse. Figure 4 shows the relation between the radial pressure gradient at the resonant surface and D_I, where the gradient is the derivative of the beta with respect to a normalized minor radius. It should be noted that the data in Fig.4 consist of the same discharges' data in Fig.3 and the symbols denote the same with Fig.3. It is found that D_I tends to increase with the increase of pressure gradient in all phases, and the gradient of phase (III) is smaller than phase (II). In these discharges, the electron temperature T_e profile has a wide flattening region around the resonant surface just after the collapse in phase (IV) shown in Fig.2. In addition, the small flattening region of T_e profile appears before the collapse, in the phase (III). As one of the reasons why D_I becomes small before the collapse, it is considered that the radial pressure gradient at the resonant surface decreases by the growth of m/n =1/1 interchange mode in the phase (III), which means that the linear and the local index D_I are not available during the growing phase of the interchange mode with a flattening T_e profile, when the non-linear effect is expected to be too large.

Figure 5 shows the dependence of an instability index of the tearing instability, Δ', on the normalized plasma current by B_t in order to check the possibility whether the tearing mode instabilities is unstable, because the locked-mode-like instability is observed in the discharge with the relatively large toroidal current. It should be noted that the data in Fig.5 consist of the same discharges' data in Fig.3 and the symbols denote the same with Fig.3. It should be noted that Δ' is evaluated by the outer solution of the vortex equation (3) [21].

$$\left(\mathbf{B}_0\cdot\nabla\right)\nabla_\perp^2\tilde{\psi}+\nabla\tilde{\psi}\times\mathbf{e}_\phi\cdot\nabla j_{\phi 0}=0\,,\quad j_{\phi 0}=\nabla_\perp^2\psi_{J0} \tag{3}$$

Here $\tilde{\psi}$ is the fluctuation of the poloidal flux, $j_{\phi 0}$ denotes the toroidal plasma current and $\mathbf{B}_0$ is the equilibrium magnetic field. It should be noted that we ignore the finite beta effects. In the phase (I), the value of Δ' is negative. In the phases (II) and (III), the values of Δ' are positive and marginally positive, respectively. The results suggest a possibility that the tearing instability is unstable in the phases (II) and (III). From Figs.3, 4 and 5, there is a possibility that, in the phase (II), both the ideal interchange modes and the tearing mode would be unstable. It should be noted that the plasma with the local maxima of Δ' at I_p/B_t~30kA has a more peaked current profile compared with other discharges because the current ramping-up rate is different due to the different neon gas-puffing timing from other cases.

To identify which mode is more dominant in the phase (II), we perform a global linear MHD stability analysis by using the following reduced MHD equation with a cylindrical geometry, (ρ, θ, ϕ) [22].

$$\rho_m\frac{\partial}{\partial t}\nabla_\perp^2\tilde{U}=-\left(\mathbf{B}_0\cdot\nabla\right)\nabla_\perp^2\tilde{\psi}-\nabla\tilde{\psi}\times\mathbf{e}_\phi\cdot\nabla j_{\phi 0}-\mathbf{e}_\phi\times\boldsymbol{\kappa}_\rho\cdot\nabla\tilde{p} \tag{4}$$

$$\rho_m\frac{\partial\tilde{\psi}}{\partial t}=\mathbf{B}_0\cdot\nabla\tilde{U}-\eta\nabla^2\tilde{\psi} \tag{5}$$

$$\frac{\partial\tilde{p}}{\partial t}+\nabla\tilde{U}\times\mathbf{e}_\phi\cdot\nabla p_0=0 \tag{6}$$

Here, $\tilde{U}$ and $\tilde{p}$ are the fluctuations of the electric potential and the pressure, the suffix '0' means equilibrium, and ρ_m and η are the mass density and the resistivity, respectively. The equilibrium pressure profile, the rotational transform and the plasma current profile are based on the MHD equilibrium reconstruction with the measurement data. The normal curvature, $\boldsymbol{\kappa}_\rho$, is evaluated from the above MHD equilibrium using the following equation, which includes a 3D geometrical effect [14].

$$\boldsymbol{\kappa}_\rho=\frac{\mathrm{d}\Omega}{\mathrm{d}\rho}\mathbf{e}_\rho \tag{7}$$

$$\Omega(\rho) \sim \Omega_t(\rho)\left(1+\Omega_h(\rho)\right) \quad (8)$$

$$\Omega_t(\rho) = \int\left(\frac{R(\rho,\theta,\phi)}{R_0}\right)^2 \mathrm{d}\theta\mathrm{d}\phi\,,\ \ \Omega_h(\rho) = \frac{N\varepsilon^2}{2\pi\ell}\frac{1}{\rho^2}\frac{\mathrm{d}}{\mathrm{d}\rho}\left(\rho^4\iota\right) \quad (9)$$

Here R and R_0 are the major radial location of the magnetic surfaces and the magnetic axis, and N, ε, ℓ and ι denote the toroidal period number, the pole number, the inverse plasma aspect ratio and the rotational transform, respectively.

Figure 6 shows the local linear stability analysis status of the discharges with the locked-mode-like instabilities, which shows that data in the phase (II) are in the region with D_I>>0.3 and Δ'>0. Here all data in Fig.6 are the same as those in Figs. 3(b) and 5. We analyze the property of the global linear MHD instability of the plasmas shown by '#105402t3.9s', '#105401t3.9s' and '#105401t4.2s' in Fig.6 as typical operational conditions for the locked-mode-like instabilities. It should be noted that Reynolds number for the typical operating conditions is around 10^7.

Figure 7 shows the radial profiles of the beta and rotational transform, $\iota_{total}/2\pi$ (red line) of '#105402t3.9s' in Fig.6. In Fig.7(b), the plasma current profile (black dotted line), which is consistent with MSE measurement, and the rotational transform profile by the plasma current and under the assumption that the plasma current is zero, $\iota_{current}/2\pi$ (blue line) and $\iota_{coil}/2\pi$ (green line), are plotted together. Here we investigate the behavior of the Magnetic Reynolds number, S, dependence on the largest linear growth rate of the calculated m/n=1/1 mode, γ, the radial structure of the electric potential fluctuation and the Sydum parameter D_s [23] when we change the plasma central beta value, β_0, and the central rotational transform due to the plasma current, ι_{j0}, keeping the same relative profiles with the experimental ones as shown in Fig.7. Here D_s is defined as the following equation.

$$D_s = -\frac{\beta'\Omega'}{\left(\varepsilon\rho\iota'/2\pi\right)^2} - \frac{1}{4}, \quad (10)$$

where ' denotes the derivative respect to ρ. The 1st and 2nd terms of the right-hand side of eq.(10) are corresponding to the 2nd and the 1st terms of the right-hand side of eq.(1), respectively. Figure 8(a) shows the contours of the Magnetic Reynolds number dependence on the growth rate. Figure 8(b) shows the boundary of the parity in the electric potential fluctuation and the contours of the Sydum parameter. Here the Magnetic Reynolds number dependence on the growth rate is evaluated from the growth rates with five Magnetic Reynolds numbers between $10^{6.9}$ and 10^7. In Figs 8(a) and (b), if the ideal interchange mode is dominant, $\gamma \sim S^0$, the parity of the radial profile around the resonant surface of $U^{\sim}$ is even and D_s>>0 [24]. If the resistive interchange mode is dominant, $\gamma \sim S^{-0.33}$ and the parity of $U^{\sim}$ is even [24]. If the tearing mode is dominant, $\gamma \sim S^{-0.6}$ and the parity of $U^{\sim}$ is odd [21].

The data point '#105402t3.9s' in Fig.6 corresponds to the '*' in Figs.8(a) and (b). Then we can identify that the ideal interchange mode is dominant in the case of the data point '#105402t3.9s' in Fig.6. This result is consistent with the radial mode structure evaluated by the SX measurement [4, 10] as shown in Fig.9. Figure 9 shows the radial profile of the radial displacement and its phase measured by the SX system for the same discharge with Fig.2. According to similar analyses on the data points '#105401t3.9s' and '#105401t4.2s' in Fig.6, the ideal interchange modes are also dominant. Then the precursors in the phase (II) of the locked-mode-like instabilities are the ideal interchange mode dominant.

4. Discussion

Here we discuss the reason why D_I in the phase (II) is larger than 0.3 as shown in Fig.3. Figure 10 shows the magnetic shear of the total rotational transform and that due to plasma current around the resonant surface during the phases (I)-(III). It should be noted that the data in Fig.11 consists of the same discharges' data in Fig.3 and the symbols denote the same with Fig.3. The total magnetic shear roughly decreases as the phase changes from (I) to (III). On the other hand, the magnetic shear due to the plasma current is much smaller than the total magnetic shear. During the phase (II), some magnetic shears due to the current enhance the total shears, and the others reduce them. From the above, the magnetic shear effect due to the plasma current on D_I would be small.

Figure 11 shows the beta gradients at the $\iota/2\pi=1$ resonant surface as the function of the normalized plasma current by B_t. It should be noted that the data in Fig.11 consists of the same discharges' data in Fig.3 and the symbols denote the same with Fig.3. The beta gradient tends to increase with the increase of the plasma current up to the initial phase of phase (II). After the middle phase of phase (II), the gradient decreases with the increase of I_p. Next, figure 12 shows the beta gradients at the normalized minor radius which the 1/1 mode resonates in the case of zero plasma current, against the plasmas having the same beta profiles with those in Fig.11. Here it should be noted that the horizontal axis is still the normalized plasma current as the same in Fig.11, but that the resonant surfaces in Fig.12 are evaluated under the assumption that the plasma current is zero. From the comparison between Figs.11 and 12, the beta gradient in the phase (II) of the experiments is much larger than that under the assumption with zero plasma current. Figure 13 shows the location of the resonant surfaces in the experiments, and the location under the assumption with zero plasma current are also shown by the hatched region, where the locations are almost the same. It should be noted that the data in Fig.13 consists of the same discharges' data in Fig.3 and the symbols denote the same with Fig.3, and that the plasma with the $\iota/2\pi=1$ location at $\rho\sim0.5$ has the more peaked current profile comparing with other discharges such as the local maxima of Δ' in Fig.5. It is found that the locations in the experiments are more inner side than those under assumption with zero plasma current in the phase (II), which leads to the large D_I in the phase (II) because the pressure gradient increases as the inner plasma region. Figure 14 shows D_I under the assumption with zero plasma current. It should be interesting that D_I is less than 0.2 even in the phase (II) under the assumption that plasma current is zero.

5. Summary

In this paper, to study the driving mechanism of the locked-mode-like instability in the LHD, we numerically analyze a linear MHD instability. In order to perform an accurate numerical analysis, the MHD equilibria consistent with the experiments should be reconstructed because in the discharges with the locked-mode-like instabilities the relatively large plasma current exists, and the property of the MHD stability strongly depends on the MHD equilibria. Here the plasma current profile is identified by the MSE diagnostics.

The discharge with the locked-mode-like instability is divided into the following 4 phases. First, the precursor hardly appears; the phase (I). Next, the precursor clearly appears, and its amplitude is almost constant; the phase (II). Then, the amplitude of the precursor increases, and the beta value gradually decreases; the phase (III). Finally, the non-rotating magnetic fluctuation rapidly grows, and the beta value also rapidly decreases; the phase (IV). In the phases (III) and (IV), the flattening region of the electron pressure appears. Then, in the phases (I) and (II), the linear MHD analysis is available. At first, we investigate the MHD stability properties of the locked-mode-like instabilities based on a local MHD analysis by using Mercier parameter, D_I, and the stability index of the tearing mode, Δ'. In the phase (I), both the ideal interchange mode and the tearing mode are stable. In the phase (II), both the ideal interchange mode and the tearing mode are unstable. To identify which instability is dominant, we apply the global linear MHD analysis based on the reduced MHD equation. From the dependence of the linear growth rate on Magnetic Reynolds number, the radial mode structure of the electrostatic potential fluctuation and other indices, the instability with the largest linear growth rate is found to be in the region where the ideal interchange mode is dominant. That is consistent with the radial mode structure evaluated by the SX measurement.

Moreover, in the phase (II), the value of D_I greatly exceeds 0.3 at the resonant surfaces. According to earlier works on the quasi-steady discharges [19, 20], D_I hardly exceeds 0.3. On the contrary, in the transient phenomena such as just after pellet injection, large MHD activity appears and D_I exceeds 0.3 [25]. Therefore, it is indicated that $D_I>>0.3$ is effective as an index of the on-set condition of the minor collapse. From the analysis of the relationships among D_I, pressure gradient and magnetic shear, the reason why D_I exceeds 0.3 in the locked-mode instability is that the resonant surface moves to the inner region, where the plasma pressure gradient is larger than that in the outer region, due to the increase of the plasma current.

Here we focus on the driving mechanism of the locked-mode-like instabilities with the interchange type mode structure. In the LHD, we also observe the locked-mode-like instabilities with the tearing

type mode structure [8, 9, 10]. The analysis of the mode is one of the important future subjects. Moreover, we focus on the MHD characteristics during the precursor phase of the locked-mode-instability because we apply a linear MHD analysis in this paper. In principle, the linear theory is available for the phase of no-MHD activities or the on-set phase of MHD activities. However, the results analyzed by the linear theory give an index to categorize the status of the plasmas obtained in the experiment. The results would be a trigger to study the non-linear behavior by the numerical calculation and/or an empirical scaling. In order to investigate the mechanism of the slowing-down of the frequency and the collapse, we should apply a non-linear analysis taking plasma flow and wall effects into account. This is another of the important future subjects.

Acknowledgments

This work was supported in part by JSPS KAKENHI (No.25289342), by NIFS under contracts NIFS07KLPH004 and by a dispatch grant from the Future Energy Research Association. The authors are grateful to the LHD Operation Group for their excellent technical support.

References

[1] Takeiri Y. *et al*., 2017 Nucl. Fusion **57** 102023.
[2] Sakakibara S. *et al*., 2002 Plasma Phys. Control Fusion **44** A217.
[3] Sakakibara S. *et al*., 2006 Fusion Sci. Technol. **50** 177.
[4] Takemura Y. *et al*., 2012 Nucl. Fusion **52** 102001.
[5] Hender T.C. *et al*., 2007 Nucl. Fusion **47** S128.
[6] Sakakibara S. *et al*., 2013 Nucl. Fusion **53** 043010.
[7] Sakakibara S. *et al*., 2015 Nucl. Fusion **55** 083020.
[8] Tokuzawa T. *et al*., 2017 Nucl. Fusion **57** 076003.
[9] Takemura Y. *et al*., 2017 Plasma Fusion Res. **12** 1402028.
[10] Takemura Y. *et al.*, 2019 Nucl. Fusion **59** 066036.
[11] Sakakibara S. *et al*., 2010 Fusion Sci. Technol. **58** 176.
[12] Sakakibara S. *et al*., 2010 Fusion Sci. Technol. **58** 471.
[13] Ida K. *et al*., 2010 Fusion Sci. Technol. **58** 383.
[14] Nakamura Y. *et al*., 1989 J. Phys. Soc. Japan **58** 3157.
[15] Hirshman S.P., Van Rij W.I. and Merkel P., 1986 Comput. Phys. Commun. **43** 143.
[16] Komori A. *et al*., 2009 Nucl. Fusion **49** 104015.
[17] Toi K. *et al*., 2010 Fusion Sci. Technol. **58** 61.
[18] Sakakibara S. *et al*., 2017 Nucl. Fusion **57** 066007
[19] Watanabe K.Y. *et al*., 2004 J. Plasma Fusion Res. ser. **6** 523.
[20] Watanabe K.Y. *et al*., 2005 Nucl. Fusion **45** 1247.
[21] Wesson J., 2011, in Chap.6 of "Tokamaks(FOURTH EDITION)" Chap. (Oxford: Oxford University Press).
[22] Strauss H.R., 1980 Plasma Phys. **22** 733.
[23] Sydum B. R., 1958 in *Proc*. of *2nd UNIC on the Peaceful Use of Atomic Energy*, UN, Geneva, **31** 157.
[24] Wakatani M., 1998 in Chap.5 of "Stellarator and Heliotron Devices" (Oxford: Oxford University Press).
[25] Yamada H. *et al*., 2010 Contrib. Plasma Phys. **50** 480.

Figure caption

Figure 1
Profile of (a) electron temperature, (b) current density, (c) rotational transform $\iota/2\pi$ and (d) Mercier parameter D_I just before beta collapse.

Figure 2
Temporal evolution of (a) volume averaged beta $<\beta>$, the ratio of plasma current Ip and toroidal magnetic field B_t, (b) electron temperature at the plasma center T_{e0}, line averaged electron density, (c) amplitude and (d) frequency of m/n = 1/1 mode estimated from poloidal magnetic fluctuation, (e) radial magnetic fluctuation amplitude measured by saddle loops and (f) Mercier parameter D_I at the $\iota/2\pi = 1$ surface.

Figure 3
(a) Amplitude of $m/n = 1/1$ mode and (b) Mercier parameter D_I versus the ratio of plasma current and toroidal magnetic field.

Figure 4
Mercier parameter D_I versus the pressure gradient at $\iota/2\pi = 1$ surface.

Figure 5
Unstable index of the tearing mode Δ' versus the ratio of plasma current and toroidal magnetic field.

Figure 6
Unstable index of the tearing mode Δ' versus Mercier parameter D_I.

Figure 7
Radial profiles of the beta and rotational transform of '#105402t3.9s' in Fig.6.

Figure 8
(a) Contours of the Magnetic Reynolds number S dependence on the growth rate γ, as like $\gamma \sim S^{\alpha}$. (b) boundary of the parity in the electric potential fluctuation $U^{\sim}$ and the contours of the Sydum parameter, D_s.

Figure 9
Radial profile of the radial displacement and its phase measured by the SX system for the similar discharge with Fig.2. Solid and dashed lines correspond to the radial displacement and its phase, respectively.

Figure 10
Magnetic shear of the total rotational transform and that due to plasma current around the resonant surface during the phases (I)-(III).

Figure 11
Pressure gradient versus the ratio of plasma current and toroidal magnetic field.

Figure 12
Pressure gradient versus the ratio of plasma current and toroidal magnetic field under the assumption of the currentless.

Figure 13

Minor radial location of $\iota/2\pi = 1$ surface versus the ratio of plasma current and toroidal magnetic field. The hatched region corresponds to the location under the assumption of the currentless.

Figure 14
Mercier parameter D_I versus the ratio of plasma current and toroidal magnetic field under the assumption of the currentless.

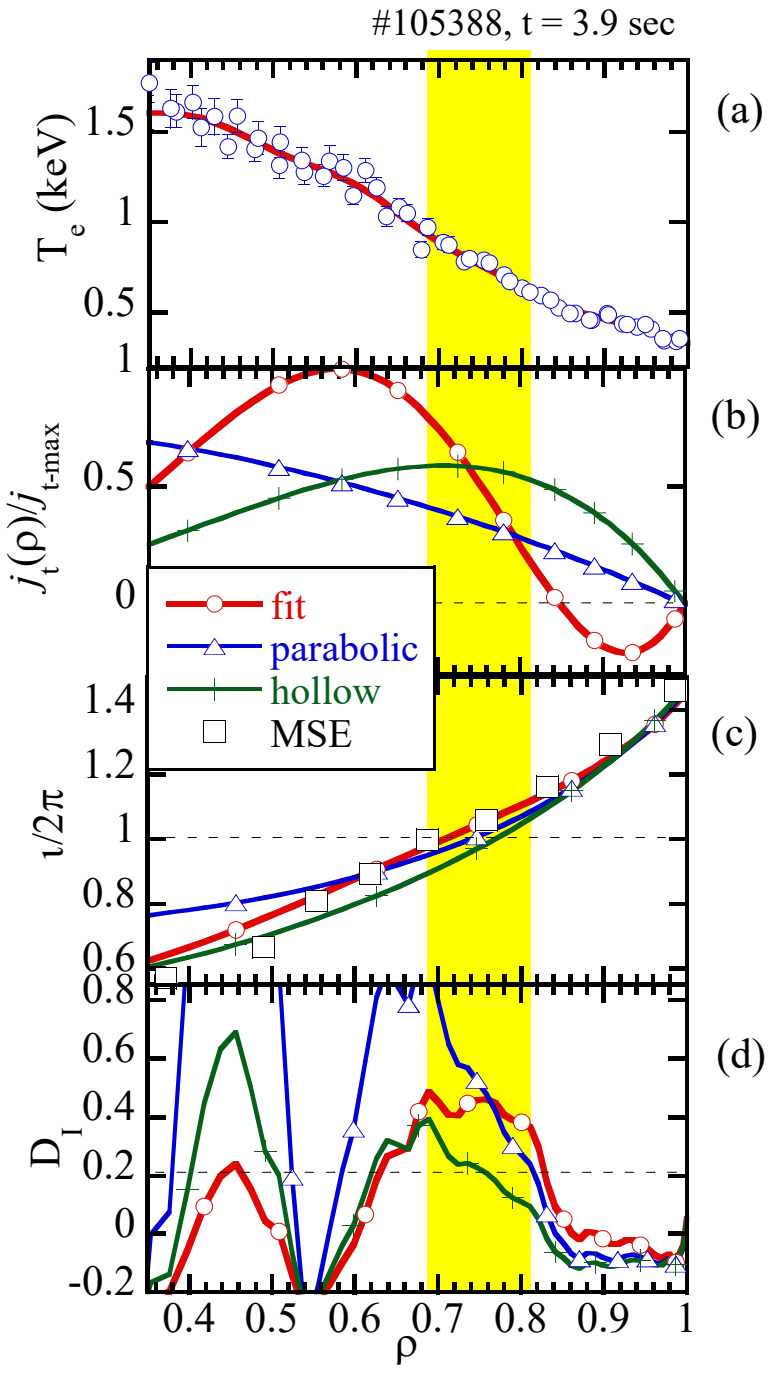

Fig.1

Profile of (a) electron temperature, (b) current density, (c) rotational transform $\iota/2\pi$ and (d) Mercier parameter D_I before beta collapse.

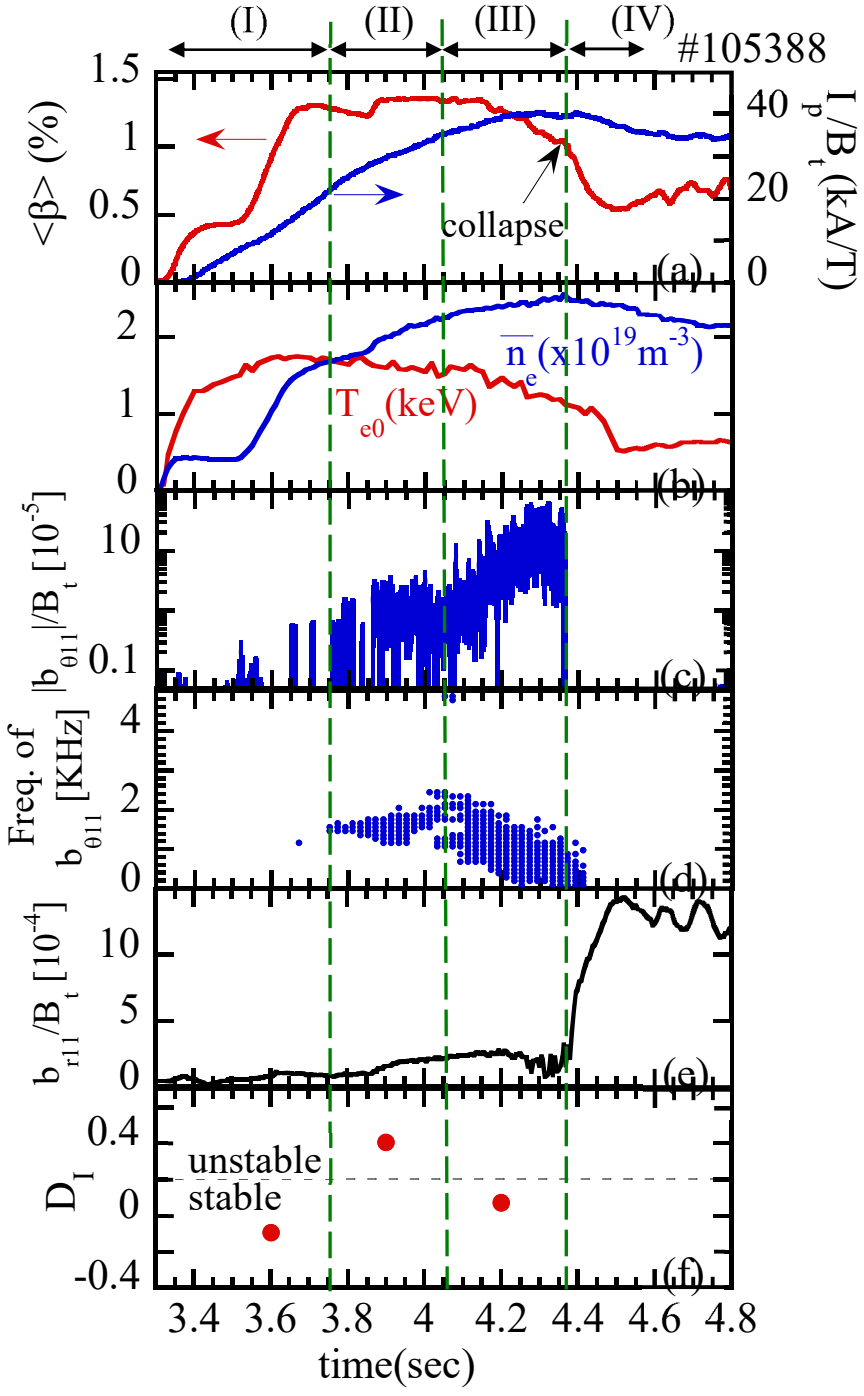

Fig.2

Temporal evolution of (a) volume averaged beta <β>, the ratio of plasma current Ip and toroidal magnetic field B_t, (b) electron temperature at the plasma center T_{e0}, line averaged electron density, (c) amplitude and (d) frequency of m/n = 1/1 mode estimated from poloidal magnetic fluctuation, (e) radial magnetic fluctuation amplitude measured by saddle loops and (f) Mercier parameter D_I at the $\iota/2\pi = 1$ surface.

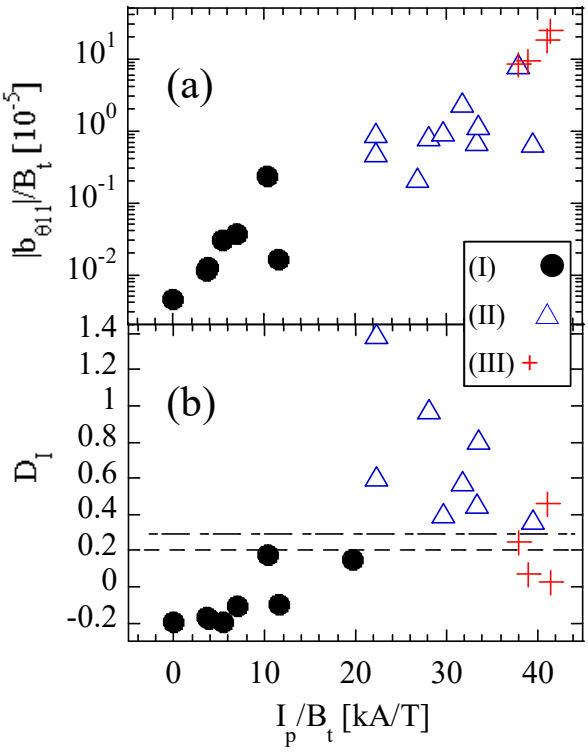

Fig.3

(a) Amplitude of m/n = 1/1 mode and (b) Mercier parameter D_I versus the ratio of plasma current and toroidal magnetic field.

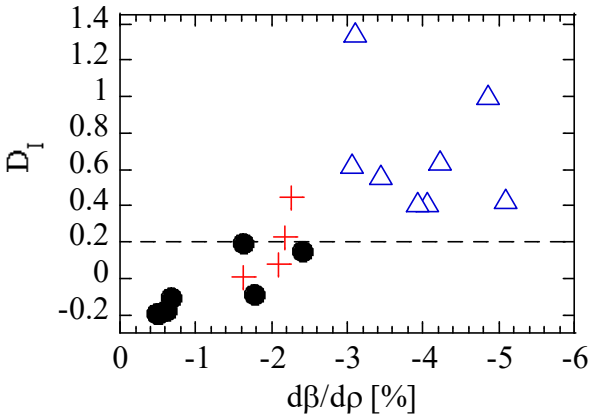

Fig.4

Mercier parameter D_I versus the pressure gradient at $\iota/2\pi$ = 1 surface.

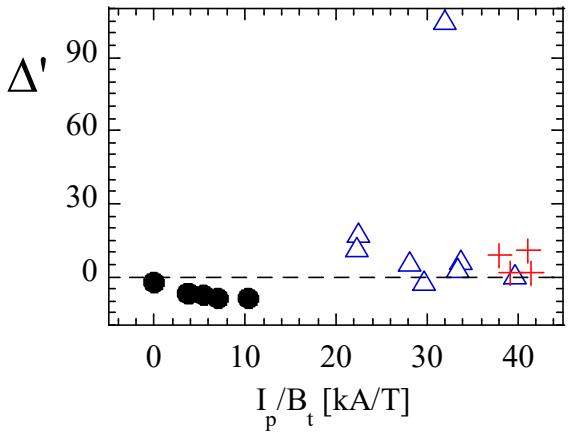

Fig.5

Unstable index of the tearing mode Δ' versus the ratio of plasma current and toroidal magnetic field.

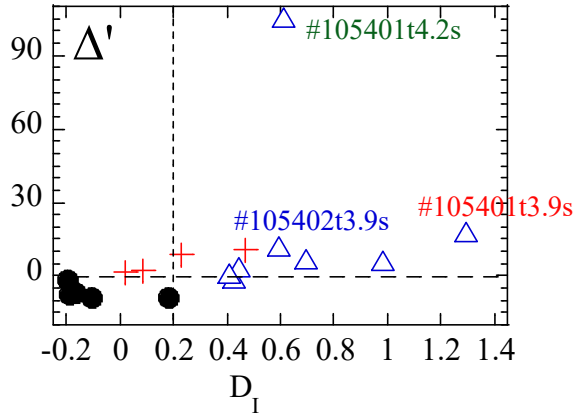

Fig.6

Unstable index of the tearing mode Δ' versus Mercier parameter D_I.

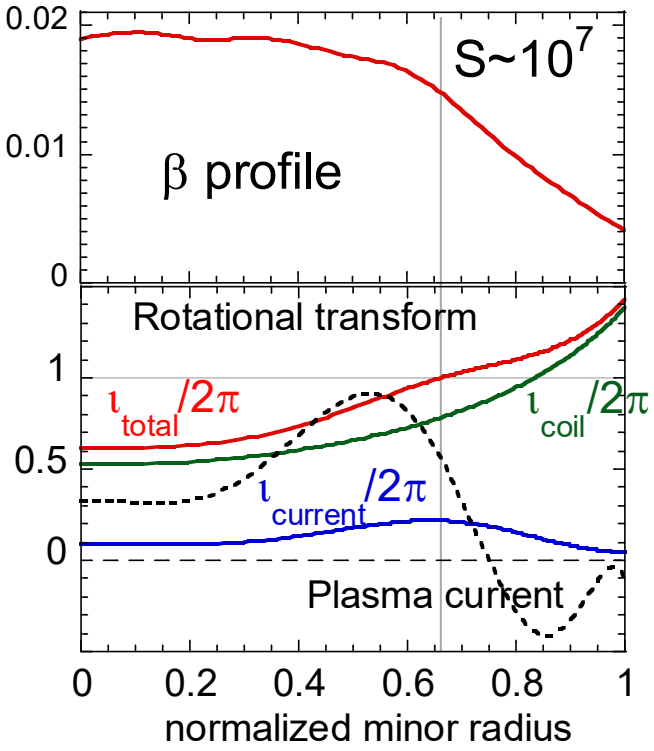

Fig.7

Radial profiles of the beta and rotational transform of '#105402t3.9s' in Fig.6.

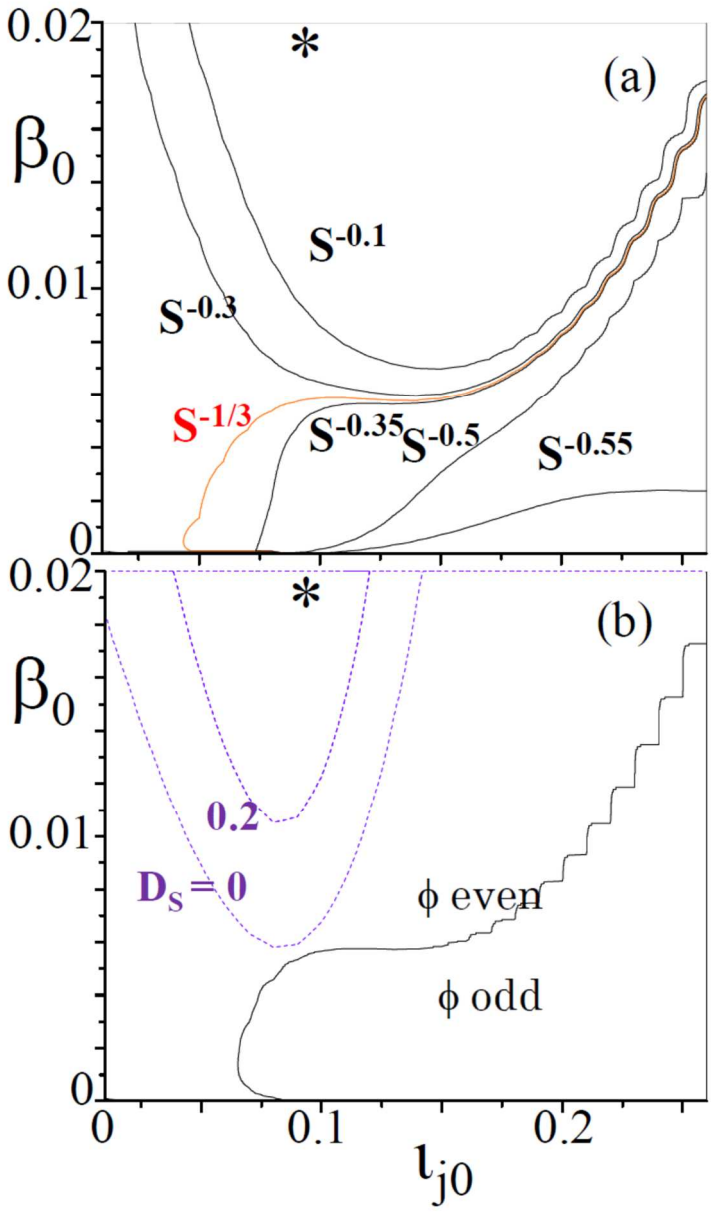

Fig.8

(a) Contours of the Magnetic Reynolds number S dependence on the growth rate γ, as like $\gamma \sim S^{\alpha}$. (b) boundary of the parity in the electric potential fluctuation U^{-} and the contours of the Sydum parameter.

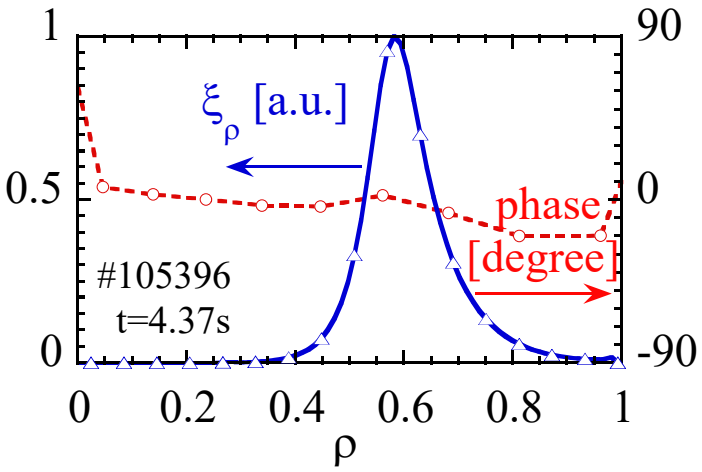

Fig.9

Radial profile of the radial displacement and its phase measured by the SX system for the similar discharge with Fig.2. Solid and dashed lines correspond to the radial displacement and its phase, respectively.

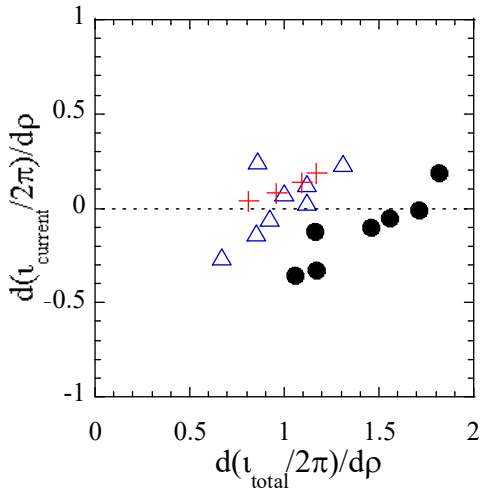

Fig.10

Magnetic shear of the total rotational transform and that due to plasma current around the resonant surface during the phases (I)-(III).

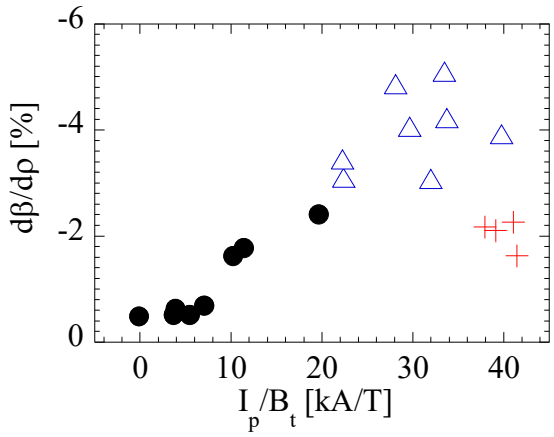

Fig.11

Pressure gradient versus the ratio of plasma current and toroidal magnetic field.

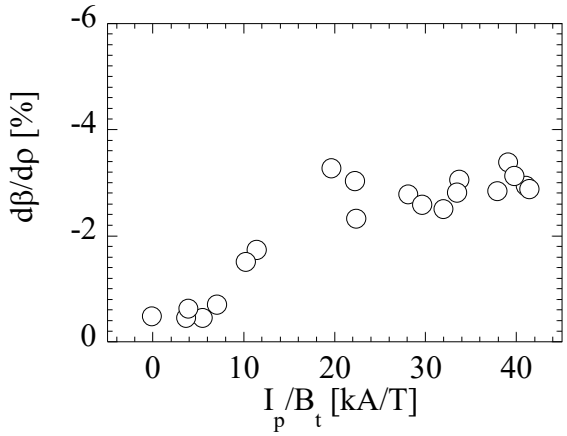

Fig.12

Pressure gradient versus the ratio of plasma current and toroidal magnetic field under the assumption of the currentless.

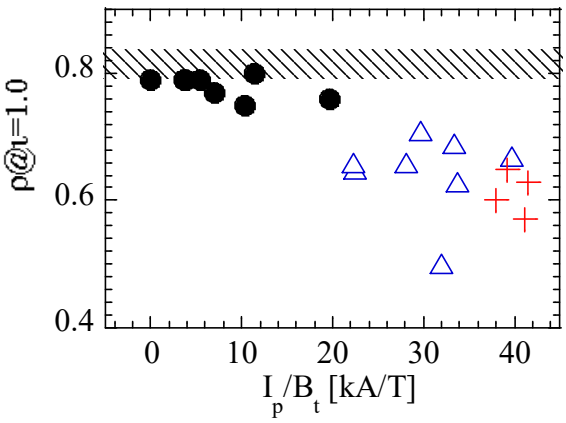

Fig.13

Minor radial location of $\iota/2\pi = 1$ surface versus the ratio of plasma current and toroidal magnetic field. The hatched region corresponds to the location under the assumption of the currentless.

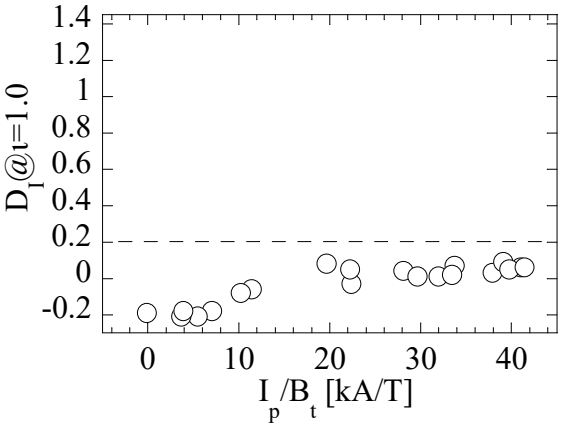

Fig.14

Mercier parameter D_I versus the ratio of plasma current and toroidal magnetic field under the assumption of the currentless.